Journal of Global Positioning Systems (2026)
Vol. 22, Issue 1: 99-113
DOI:10.5081/jgps.22.1.99

2026
© CPGPS
Journal of Global Positioning Systems

Short-term Forecasting and Integrity Overbounding of Low-Latitude Ionospheric Scintillation

Hao Liu, Dongsheng Zhao*, Kefei Zhang, Ke Xu, Qichen Zhao

School of Environment and Spatial Informatics, China University of Mining and Technology, Xuzhou 221116, China

Corresponding author: Dongsheng Zhao <dszhao@cumt.edu.cn>

Abstract: Ionospheric scintillation is a major error source that constrains high-accuracy and high-integrity positioning services of the BeiDou Navigation Satellite System (BDS) in low-latitude regions. Its evolution is characterized by strong non-stationarity, abrupt variation, and complex spatiotemporal coupling. In particular, under geomagnetic disturbances or intense solar activity, scintillation can induce rapid carrier-phase fluctuations and increase the probabilities of cycle slips and loss of lock, thereby significantly degrading positioning accuracy, availability, and integrity. Although existing studies have achieved encouraging results in scintillation forecasting, most of them mainly focus on numerical prediction itself, while the continuous evolution of scintillation risk and its integrity-oriented overbounding characterization remain insufficiently investigated. To address this issue, this study proposes a joint framework for multi-step forecasting of ionospheric scintillation risk and construction of an integrity envelope by combining a Cascade long short-term memory (Cascade LSTM) network with a radial basis function (RBF) model. The Cascade LSTM is first used to extract the low-frequency evolutionary trend embedded in the scintillation time series, and the RBF model is then employed to characterize the conditional mean and variance of the prediction residuals. In this way, the proposed method enables the synchronous generation of continuous multi-step scintillation-risk forecasts and a corresponding overbounding envelope, providing model support for integrity-constrained applications under disturbed ionospheric conditions. Experiments were conducted using low-latitude scintillation observations from 16 to 25 March 2024, including a significant geomagnetic storm event on 24 March, to evaluate the predictive performance of the model during both scintillation-active and quiet periods. The results show that, in six-step forecasting on the test set, the proposed Cascade LSTM + RBF model outperforms the conventional recursive LSTM model, with average reductions of approximately 3.8%, 2.5%, and 2.3% in e_{MAE}, e_{RMSE}, and e_{NRMSE}, respectively. CDF-based envelope analysis and Stanford-plot assessment further demonstrate that the proposed model can adaptively widen the overbounding envelope during scintillation-active intervals while maintaining a tight overbounding envelope during quiet intervals, with most residuals remaining within the envelope bounds, indicating favorable integrity-assessment capability. These results suggest that the proposed method can effectively support short-term forecasting and early warning of low-latitude ionospheric scintillation, and provide a foundation for constructing a tight overbounding envelope for trustworthy positioning in low-latitude GNSS applications.

Keywords: Global Navigation Satellite System; Ionospheric Scintillation; Long-Term Sequence Forecasting; Integrity overbounding envelope.

1 Introduction

The low-latitude ionosphere is strongly influenced by solar activity and geomagnetic forcing. Around local sunset, it becomes particularly susceptible to the Rayleigh-Taylor instability, which promotes the development of plasma bubbles (Pi et al., 1997; Zhao et al., 2022, 2024). When GNSS signals propagate through the resulting plasma irregularities, diffraction and refraction produce ionospheric scintillation. Scintillation increases carrier-phase noise and induces rapid phase fluctuations, thereby increasing the likelihood of cycle slips and loss of lock (Chen et al., 2017; Kim et al., 2014; Luo et al., 2020; Oljira, 2023; Wang and Morton, 2017; Zhao et al., 2019). Under severe conditions, these effects can compromise the stable provision of positioning, navigation, and timing services in low-latitude regions (Li et al., 2024; Vadakke Veettil and Aquino, 2021). Consequently, numerous studies have investigated methods for improving GNSS positioning accuracy and integrity under scintillation conditions (De Lima et al., 2015; Sridhar et al., 2017; McGranaghan et al., 2018; Carvalho et al., 2022).

In recent years, machine-learning and deep-learning methods have further advanced ionospheric scintillation and ionospheric-variability forecasting. For instance, decision-tree-based machine-learning models have been used to detect amplitude scintillation from geodetic GNSS receivers (Li et al., 2024), ConvGRU networks have been introduced to predict scintillation using ground-based GNSS observations across South America (Atabati et al., 2024), and neural-network models based on geodetic GNSS measurements have been applied to ROTI-based scintillation prediction over Africa (Tete et al., 2024). More recently, Gao et al. (2025) developed ISNet, a decomposed dynamic spatiotemporal neural network capable of forecasting the regional amplitude scintillation index S4 one hour in advance. Ojo et al. (2025) employed a long short-term memory network to forecast ROTI-defined ionospheric irregularities over equatorial and low-latitude regions. These studies demonstrate the increasing capability of deep-learning models to capture the nonlinear temporal and spatial evolution of ionospheric disturbances. Recent research has also begun to consider probabilistic forecasting and uncertainty representation. Mao et al. (2025) developed a deep-ensemble neural-network framework for global VTEC mapping that simultaneously provides ionospheric estimates and their associated uncertainty. Monte-Moreno et al. (2026) proposed a Bayesian probabilistic model for global ROTI forecasting based on the heavy-tailed statistical characteristics of ionospheric disturbances, providing probabilities of ROTI exceeding specified thresholds for forecast horizons ranging from 30 min to 6 h. These developments indicate that data-driven ionospheric modeling is progressing from event classification and deterministic time-series prediction toward nonlinear spatiotemporal modeling and uncertainty-aware forecasting. Nevertheless, existing uncertainty-aware studies have mainly focused on large-scale ionospheric parameters or the probability of disturbance occurrence. Scintillation-specific prediction-error modeling, integrity-oriented uncertainty calibration, and statistically validated overbounding-envelope construction for GNSS applications remain insufficiently investigated.

Despite recent progress, low-latitude ionospheric scintillation remains highly non-Gaussian, time-varying, and susceptible to abrupt disturbances. If a forecasting model underestimates scintillation intensity during extreme geomagnetic or solar activity, the associated positioning risk may also be underestimated, thereby compromising service availability and safety. Safety-critical applications, including autonomous driving, unmanned aerial vehicle navigation, and urban air mobility, require not only accurate scintillation forecasts but also tight overbounding envelopes that support positioning-integrity assessment. Several overbounding methods have been developed to characterize the tail behavior of practical error distributions. Nikiforov (2019) established the relationship between GNSS pseudorange overbounding models and integrity-risk overbounds, examined conservative solution procedures, and developed methods for computing vertical and horizontal integrity-risk components. Zhang et al. (2021) proposed an improved paired-overbounding method for ranging errors that relaxes conventional Gaussian assumptions, including zero mean, symmetry, and unimodality, and transforms the error distribution into a Gaussian-equivalent form.

However, ionospheric scintillation varies rapidly, and traditional statistical methods alone are insufficient to accurately characterize the heavy-tailed and asymmetric distribution of model forecasting errors. Therefore, constructing a tight overbounding envelope for ionospheric scintillation forecasting is essential, especially under severe geomagnetic storms or extreme solar activity, so as to avoid abrupt degradation of positioning integrity caused by forecast mismatch. In this study, a Cascade LSTM model is employed to perform short-term forecasting of the ionospheric scintillation indicator, i.e., the rate of TEC index (ROTI). Then, an RBF network is used to model the prediction residuals and conditional variance of the Cascade LSTM model. In this way, both the ionospheric scintillation value and its tight overbounding envelope can be predicted in advance.

2 Data and methodology

This study investigates the forecasting of ionospheric scintillation and the construction of its corresponding tight overbounding envelope using GNSS stations located in low-latitude regions. Figure 1 illustrates the overall framework of the proposed method. First, the raw GNSS observations are preprocessed to derive the rate of TEC index (ROTI), which is used to characterize variations in station-level positioning performance. Then, a **Cascade LSTM** model is employed to forecast the temporal evolution of ROTI-related risk. Finally, based on the residuals obtained from the Cascade LSTM on the training set, an RBF model is designed to learn the relationship between space-weather variations and the forecasting residuals, thereby correcting the Cascade LSTM predictions and generating the corresponding integrity information for the ROTI forecasting product.

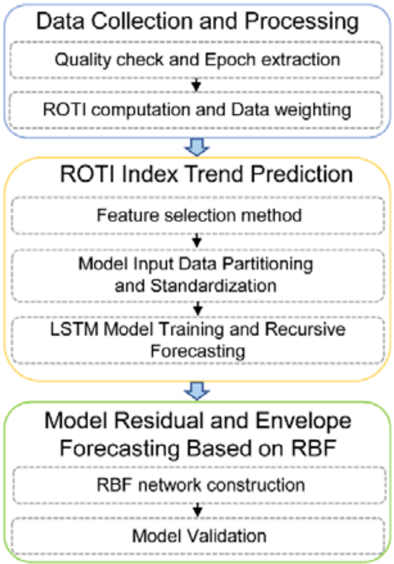

Fig. 1 Overall flowchart of low-latitude ionospheric scintillation risk forecasting and integrity overbounding envelope construction

The GPS dataset used in this study spans six years, from January 2019 to December 2025. As shown in Fig. 2, the GNSS stations used in this study are distributed in the low-latitude region of Hong Kong, China. Among these data, observations collected in March 2024 were selected for hypothesis testing and model validation. The data selection was based on the following criteria. First, at least seven consecutive days of continuous observations had to be available. Second, because the study area is located in Hong Kong, China, on the northern side of the equatorial ionization anomaly crest, months with relatively frequent ionospheric scintillation activity were preferred. Third, after excluding satellites with elevation angles lower than 30°, the scintillation-related variation had to persist for more than 1 h.

Fig. 2 Spatial distribution of GNSS stations in the study area

Because indices that directly characterize ionospheric scintillation generally require dedicated ionospheric scintillation monitoring receivers (ISMRs), direct scintillation monitoring is costly. Therefore, the **ROTI** index is widely used to characterize the scintillation-related effects induced by ionospheric irregularities. As shown in Fig. 3, although ROTI can describe the level of ionospheric activity above a station, it cannot directly reflect the degradation of geometry-related positioning conditions, such as deterioration in the dilution of precision (DOP). To address this limitation, this study further introduces a **risk index** derived from geodetic GNSS receivers to characterize positioning risk under scintillation conditions. This index is used to characterize variations in positioning risk associated with ionospheric scintillation and is defined as follow,

$$Risk = \sum_{i=1}^{n} \omega_i ROTI_i \tag{1}$$

where $ROTI_i$ denotes the ROTI value of the i-th visible satellite at epoch t, n is the number of satellites observed by the receiver at epoch t, and ω_i

represents the weight used to project the ROTI of different satellites to the ground-level positioning risk. The weighting function is given by

$$\omega_i = \frac{\exp\left[k * \left(\frac{90° - \theta_i}{90°}\right)\right]}{\sum_{j=1}^{n} \exp\left[k * \left(\frac{90° - \theta_j}{90°}\right)\right]} \tag{2}$$

where the weight assigned to low-elevation satellites is related to the multipath effect experienced by the station, and θ_i denotes the elevation angle of the line of sight between the receiver and the *i*-th satellite. In this way, the proposed risk index accounts not only for ionospheric irregularity intensity, but also for the differing impacts of individual satellites on station-level positioning performance.

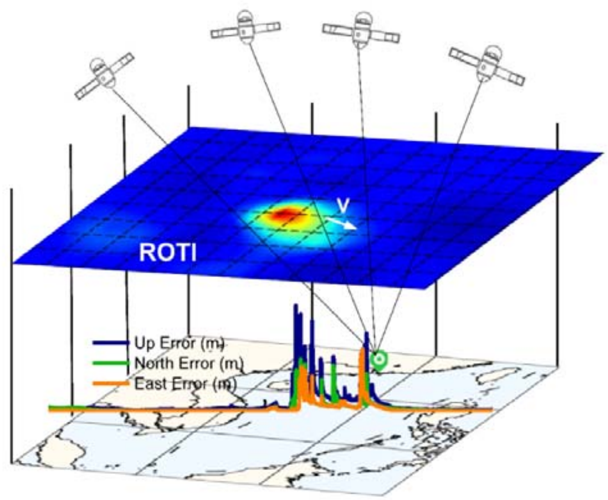

Fig. 3 Schematic illustration of the difference between ROTI-based ionospheric activity representation and positioning-geometry degradation

3 Methodology

To enable 30-min-ahead forecasting of positioning risk during ionospheric scintillation, this study develops a hybrid Cascade LSTM-RBF framework based on trend forecasting and residual modeling. By combining ROTI-related trend prediction with residual uncertainty modeling, the proposed method achieves the joint estimation of the scintillation-related risk index and its tight overbounding envelope. As shown in Fig. 4, the overall forecasting framework consists of three parts. First, a Cascade LSTM model is employed to predict the trend evolution of the ROTI-related risk index. Next, the residual between the observation and the trend prediction is calculated. Finally, an RBF model is used to characterize the conditional mean and variance of the residual under different space-weather conditions, thereby enabling the prediction of both the scintillation-related risk index and its tight overbounding envelope.

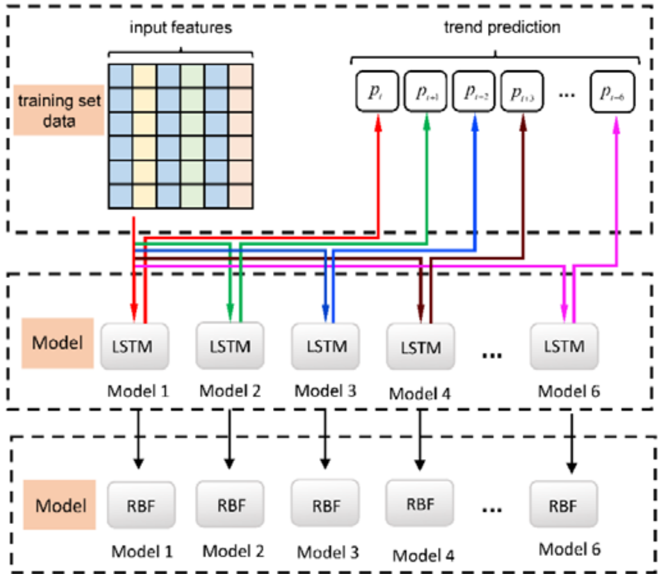

Fig. 4 Framework for ionospheric scintillation risk forecasting and tight overbounding envelope construction

The ionospheric scintillation-related risk index, obtained after elevation-angle weighting of scintillation information from different satellites, can be decomposed into multiple components represented by different models, i.e.,

$$y_t = f_{LSTM}(X_{t-1:t-L}) + \mu(x_t) + \varepsilon_t \tag{3}$$

where y_t denotes the true ionospheric scintillation-related positioning risk at epoch *t*. The first term, $f_{LSTM}(X_{t-1:t-L})$ represents the trend component learned by the Cascade LSTM model from the historical time series. The second term, $\mu(x_t)$ denotes the systematic bias component modeled by the RBF network under different space-weather conditions. The remaining term, ε_t represents the random disturbance that cannot be explained by the above two components. Here, x_t denotes the input feature vector constructed at epoch *t*, and $X_{t-1:t-L}$ denotes the historical time-series input composed of the previous *L* epochs.

3.1 Cascade LSTM neural network model

LSTM (Long Short-Term Memory) is an improved variant of the recurrent neural network (RNN) and is capable of capturing long-term dependencies in time-series data through its gated architecture (Atabati et al., 2024). It is therefore particularly suitable for modeling ionospheric scintillation-related sequences, which usually exhibit strong temporal correlation and pronounced non-stationarity (Tete et al., 2024; Xu et al., 2020). Compared with the conventional RNN structure, LSTM can alleviate the problems of vanishing and exploding gradients to a certain extent, and thus generally provides better stability and accuracy in long-sequence forecasting tasks.

The basic computation of an LSTM network involves the forget gate, input gate, candidate state update, and output gate. Let x_t denote the input vector at epoch t, and let h_{t-1} and C_{t-1} denote the hidden state and cell state at the previous epoch, respectively. The forget gate determines how much historical information should be retained, the input gate determines how much new information should be written into the memory cell, and the candidate memory state is then used to update the current cell state C_t. Finally, the output gate generates the hidden state h_t at the current epoch. Here, W and U denote the weight matrices associated with the current input and the historical memory, respectively.

To achieve multi-step trend forecasting of the ionospheric scintillation-risk sequence, this study further develops a Cascade LSTM model based on the conventional recursive LSTM framework. Suppose that the observations over the previous N time steps are used to predict the values over the next K time steps. During training, a sliding-window strategy is adopted, in which the first N time steps are used as the input and the (N+1)-th time step is used as the output to train the model. During prediction, a recursive strategy is adopted: the forecast for the first future time step is generated first, and this predicted value is then fed back into the model input to forecast the second future time step.

By repeating this procedure, the forecasts for the first to the ($K-1$)-th future time steps are sequentially used as inputs to generate the forecast for the K-th future time step. Because the inputs for later forecast steps contain model-generated predictions, the associated forecasting errors are inevitably accumulated and propagated through the recursive process, which significantly degrades long-horizon prediction accuracy.

To address this limitation, a Cascade LSTM model is proposed in this study, as shown in Fig. 5. The essential idea of the cascade strategy is to explicitly simulate the actual multi-step forecasting scenario during training by constructing a dedicated sub-model for each forecast horizon, so that the training process is consistent with the application process. Specifically, the first sub-model is constructed in the same manner as a conventional one-step model, taking the observations over the previous N time steps as input and generating the prediction for the (N+1)-th time step. This prediction then serves as a key input to the next sub-model. The second sub-model is subsequently constructed using the true observations from the 2nd to the N-th time steps together with the predicted value at the (N+1)-th time step as the input, while the true value at the (N+2)-th time step is used as the output. Similarly, the third sub-model uses the true observations from the 3rd to the N-th time steps together with the predicted values at the (N+1)-th and (N+2)-th time steps as the input, and outputs the true value at the (N+3)-th time step. Following this strategy, K sub-models can be constructed successively to predict the next K time steps.

Compared with the conventional recursive LSTM model, the Cascade LSTM model has a clear advantage in that the prediction generated by the previous sub-model is explicitly incorporated into the training input of the subsequent sub-model. In this way, the accumulation of forecasting errors can be effectively mitigated, while consistency between the training scenario and the practical application scenario is maintained. In practical use, only the observations over the previous N time steps need to be input into the overall model to obtain continuous forecasts for the next K time steps, thereby improving the stability and accuracy of multi-step forecasting.

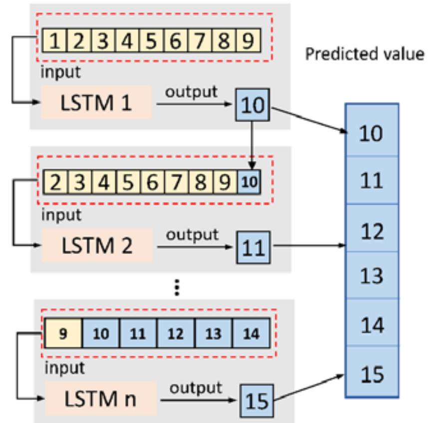

Fig. 5 Schematic illustration of multi-step forecasting using the Cascade LSTM model

3.2 RBF-based residual modeling and integrity envelope construction

Because low-latitude ionospheric scintillation is strongly affected by solar and geomagnetic activity, the prediction errors of the deep-learning model may exhibit significant systematic bias and conditional heteroscedasticity under disturbed space-weather conditions. Therefore, after obtaining the trend forecast from the Cascade LSTM model, an RBF network is introduced to characterize the statistical properties of the forecast residuals and provide a basis for integrity-oriented overbounding analysis. The RBF model is introduced not only to correct the prediction residuals of the Cascade LSTM model, but also to estimate the uncertainty of the residuals. Specifically, the RBF model learns the conditional mean and variance of the forecasting residuals under different space-weather conditions. The conditional mean is used to correct the deterministic forecast, while the conditional variance is used to construct a tight integrity overbounding envelope. Therefore, the proposed Cascade LSTM+RBF framework can simultaneously provide improved forecasting results and integrity information.

Let the residual between the observed value and the Cascade LSTM prediction at epoch t be defined as

$$\begin{aligned} e_t &= y_t - \hat{y}_t^{LSTM} \\ e_t &= \mu_t + \varepsilon_t, \varepsilon_t \sim (0, \sigma^2) \end{aligned} \tag{4}$$

where y_t denotes the observed ionospheric scintillation-related risk at epoch t, $\hat{y}_t^{LSTM}$ denotes the prediction generated by the Cascade LSTM model, and e_t is the forecast residual. The residual is further decomposed into a conditional mean component μ_t and a random disturbance component ε_t. Since the residual distribution may vary with external space-weather conditions, an RBF network is employed to characterize the conditional statistical properties of the residual.

First, the RBF model is used to estimate the conditional mean of the residual,

$$\mu_t = f_{RBF}(x_t) \tag{5}$$

where x_t denotes the feature vector at epoch t, including the relevant space-weather and historical input variables, and μ_t represents the systematic bias component of the prediction residual under the given input condition.

To quantify the residual uncertainty in a principled manner, we adopt a second RBF network that operates on the squared residual $\left((\varepsilon_t - \mu_t)^2\right)$ This network learns the conditional variance of the forecasting error, expressed as,

$$\sigma_t^2 = \mathrm{RBF}\left((\varepsilon_t - \mu_t)^2\right) \tag{6}$$

where ε_t is the actual observation at time μ_t is the preliminary mean prediction from the LSTM module, and the RBF network effectively captures the nonlinear dependence of the variance on the residual magnitude. The conditional standard deviation σ_t is then obtained as the square root of (6), providing a scale for the expected deviation.

Given this uncertainty estimate, we correct the raw LSTM forecast by adding the residual mean $\mu(x_t)$, which is the output of a first RBF network modelling the systematic bias. The final corrected forecast mean is thus,

$$\hat{y}_t = f_{\mathrm{LSTM}}(X_{t-L:t-1}) + \mu(x_t) \tag{7}$$

where $f_{\mathrm{LSTM}}(*)$ denotes the LSTM's multi-step prediction based on the past L input vectors, and $\mu(x_t)$ compensates for the deterministic part of the residual that is predictable from the current feature vector x_t

For integrity-critical GNSS applications, we construct a protection level (PL) that bounds the actual error with high confidence. The PL is defined as,

$$PL_t = k\sigma_t \tag{8}$$

where k denotes the overbounding coefficient determined through calibration under a specified integrity-risk requirement, and σ_t is the conditional standard deviation estimated from residual modeling. Accordingly, the final tight overbounding envelope of the forecasting product can be expressed as:

$$\hat{y}_t \pm PL_t \tag{9}$$

where $\hat{y}_t$ is the bias-corrected forecast from (7) and $PL_t = k\sigma_t$ is the adaptive protection level from (8), yielding a dynamically bounded envelope.

In this way, the proposed RBF-based residual modeling strategy enables the joint prediction of the forecast mean and its associated uncertainty, thereby providing not only a multi-step prediction result for ionospheric scintillation-related risk, but also a tight overbounding envelope suitable for integrity-constrained GNSS applications.

4 Experimental validation

This study uses continuous observations from 16 March to 25 March 2024 as the experimental dataset. During this period, a significant geomagnetic storm occurred on 24 March 2024**,** with the Kp index exceeding 8**,** indicating a strong storm level. This event caused remarkable variations in ionospheric parameters such as TEC and ROTI at different latitudes, reflecting the ionospheric disturbances induced by the combined effects of solar flares and geomagnetic storms. The dataset covers not only the quiet period before the disturbance but also the recovery phase afterward, thereby fully reflecting the short-term non-stationarity of the ionosphere and the complex relationships among multiple variables. Therefore, it was selected to validate the performance of the Cascade LSTM + RBF model in continuous multi-step forecasting and in capturing disturbance responses.

Figure 6 presents the temporal variations of the selected space-weather indices and the ionospheric scintillation-related risk index during the study period. To better characterize the response of ionospheric scintillation to space-weather conditions, Bz, SYM-H, and the electric field were selected as external indicators representing variations in the near-Earth space environment. The fourth panel shows the GNSS-derived scintillation-related risk index, which differs from the first three parameters because it characterizes the station-level positioning-risk response to ionospheric irregularities. Higher risk-index values indicate that scintillation-related disturbances may affect more geometry-sensitive GNSS observations and thus increase the likelihood of positioning accuracy and reliability degradation. This panel is therefore included to link the external geomagnetic disturbance conditions with the GNSS positioning-risk response. Because these variables have substantially different units and numerical ranges, directly using them as model inputs may cause features with larger magnitudes or variances to dominate the training process, thereby degrading forecasting performance.

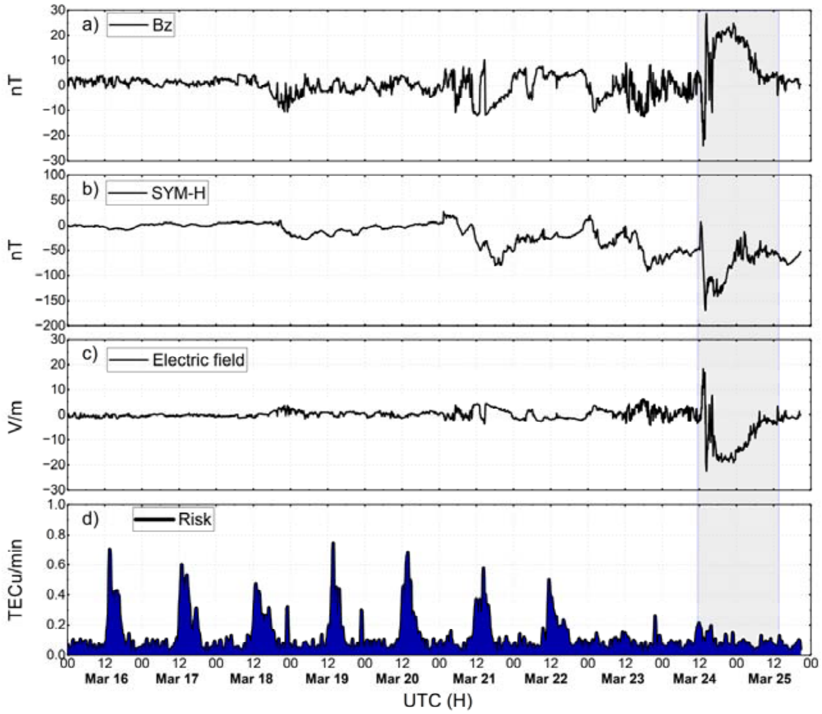

Fig. 6 Temporal variations of the selected space-weather drivers (Bz, SYM-H, and electric field) and the ionospheric scintillation-related risk index during 16-25 March 2024

Before model training, all input variables were standardized using the Z-score normalization method to reduce the influence of different physical units and numerical ranges. The standardized value was calculated as follows:

$$x_{i,j}^{'} = \frac{x_{i,j} - \mu_j}{\sigma_j} \tag{10}$$

where $x_{i,j}$ denotes the original value of the j-th variable at the i-th sample, $x_{i,j}^{'}$ is the standardized value, and μ_j and σ_j represent the mean and standard deviation of the j-th variable in the training dataset, respectively. Specifically, μ_j and σ_j are calculated as:

$$\mu_j = \frac{1}{n}\sum_{i=1}^{n} x_{i,j} \tag{11}$$

$$\sigma_j = \sqrt{\frac{1}{n-1}\sum_{i=1}^{n}\left(x_{i,j} - \mu_j\right)^2} \tag{12}$$

where n is the number of training samples. After standardization, each input variable has approximately zero mean and unit variance, rather than being constrained to the interval $[0,1]$.

After forecasting, the normalized model outputs were transformed back to their original scale so that they could be compared with the observations and used in subsequent analyses. The corresponding expression is:

$$\hat{y}_i = y_i^{*} \cdot \sigma_y + \mu_y \tag{13}$$

where $\hat{y}_i$ denotes the model prediction after inverse transformation, y_i^{*} denotes the normalized model output, σ_y and μ_y represent the mean and standard deviation of the target variable y in the training dataset, respectively.

The normalized dataset was divided into training, validation, and test sets in a ratio of 7:2:1. The training set was used for model training, and residual prediction was further performed based on the trained model. The mean squared error (MSE) was adopted as the objective function, and the network parameters were optimized using the Adam optimizer. To prevent overfitting, L2 regularization was introduced into the fully connected layer, and the corresponding objective function with the regularization term is given in Eq. (14). The parameters of the entire model were updated through backpropagation to obtain an optimal parameter set that minimizes the MSE. The Adam optimizer is a stochastic optimization algorithm based on adaptive estimation of first and second moments.

$$e_{MSE} = \frac{1}{n}\sum_{t=1}^{n}\left(p_t^{pre'} - p_t^{'}\right)^2 + \frac{\alpha}{2} w^T w \tag{14}$$

In addition, the dropout strategy was introduced to further improve model regularization. During training, part of the weights or outputs in the hidden layer were randomly set to zero, thereby reducing the interdependence among hidden neurons and enhancing the generalization capability of the neural network. Based on the above considerations, the Cascade LSTM-RBF model was adopted for multi-step forecasting. Using input features with a historical sequence length of 12, ultra-short-term forecasting of the ionospheric scintillation time series was performed from 5 min to 30 min ahead (i.e., 1-6 forecast steps). Six LSTM-RBF models with the same network architecture shared the same input features, while each model was trained independently to avoid mutual interference. The programming platform and the corresponding hyperparameter settings are listed in Table 1.

As shown in Fig. 7, the variations of eRMSE with the number of training iterations were compared for both the training set and the test set over the 5–30 min forecasting tasks (i.e., 1–6 forecast steps). It can be observed that the errors of the six LSTM sub-models on the training set decrease gradually as the number of iterations increases, while the model still exhibits good convergence behavior on the test set. These results indicate that the proposed model has strong generalization capability for ionospheric scintillation forecasting.

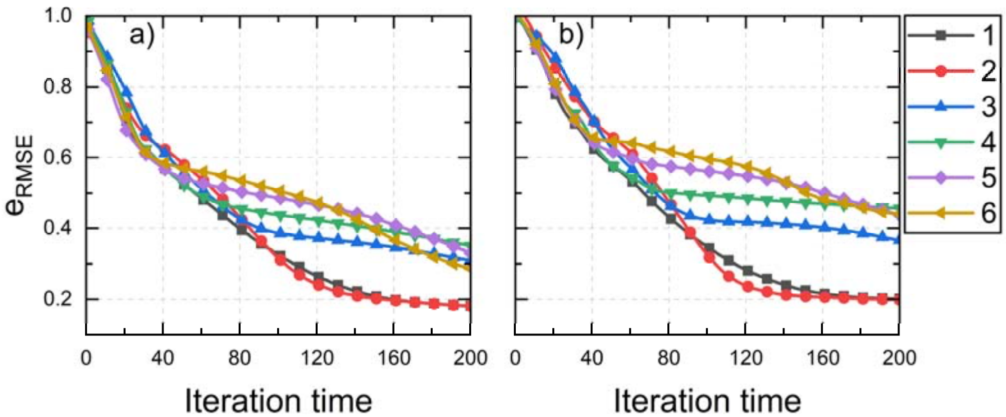

Fig. 7 Variation of the loss function on the training and test sets

To ensure the reproducibility of the proposed model, the main implementation environment and hyperparameter settings of the Cascade LSTM-RBF framework are summarized in Table 1. The model was implemented using the PyTorch platform with Python as the development language, and the main neural-network modules included LSTM, Linear, and Dropout layers. In addition, key training parameters, including the number of iterations, input time window, and number of LSTM hidden units, are listed to clarify the model configuration used in this study.

Table 1 Hyperparameter settings of the proposed model

Programming platform	**Development platform**	**functions**	**Development language**	**Basic frequency**
	PyTorch	LSTM, Linear, Dropout	Python	3.2 GHz
Parameters	**Iterations**	**Time window**	**Number of long short-term memory (LSTM) neuron**	
	200	12	64 (hidden units)	

Following the hyperparameter configuration listed in Table 1, the trained models were applied to the test set to evaluate their continuous multi-step forecasting performance. Four model schemes, namely recursive LSTM, recursive LSTM+RBF, Cascade LSTM, and Cascade LSTM+RBF, were compared under the same experimental conditions. The forecasting errors were calculated for six successive prediction horizons from 5 min to 30 min. As shown in Table 2, the proposed Cascade LSTM+RBF model generally achieves lower forecasting errors than the conventional recursive LSTM model. For example, at the 5-min prediction horizon, the eMAE and eRMSE decrease from 0.73 and 0.95 for the recursive LSTM model to 0.68 and 0.88 for the Cascade LSTM+RBF model, respectively. At the 10-min horizon, the corresponding errors decrease from 0.71 and 0.92 to

0.64 and 0.83. For the 30-min-ahead prediction, the Cascade LSTM+RBF model also maintains relatively low errors, with an eMAE of 0.61, eRMSE of 0.81, and eNRMSE of 3.31. These results indicate that the cascade forecasting strategy and RBF-based residual correction can improve the stability and accuracy of continuous multi-step ionospheric scintillation forecasting. It should be noted that the improvement in deterministic forecasting accuracy is moderate. However, the RBF model is introduced not only to improve the forecasting accuracy, but also to estimate the residual uncertainty. Based on the residual mean and variance provided by the RBF model, a tight integrity overbounding envelope can be constructed for the Cascade LSTM forecasts. Therefore, the proposed Cascade LSTM+RBF framework improves the prediction results while also providing integrity information for ionospheric scintillation-risk forecasting.

Overall, the cascade strategy outperforms the recursive strategy in multi-step forecasting. With or without RBF-based residual correction, the Cascade LSTM models generally achieve lower errors at most forecast horizons. This result indicates that horizon-specific sub-models can reduce error accumulation and propagation, thereby improving the stability of continuous multi-step forecasting.

A further comparison between the Cascade LSTM and Cascade LSTM+RBF models shows that the RBF-based residual correction further reduces the forecasting errors at most forecast horizons. In terms of the overall average over the six forecast steps, the Cascade LSTM+RBF model reduces the errors by approximately 3.8%, 2.5%, and 2.3% in eMAE, eRMSE, and eNRMSE, respectively, compared with the standalone Cascade LSTM model. This indicates that the RBF model can effectively capture the statistical characteristics of the residuals and compensate for the systematic bias not fully modeled by the main forecasting network, thereby improving multi-step forecasting accuracy.

From the stepwise results, the Cascade LSTM+RBF model exhibits relatively stable advantages at 5, 10, 15, and 30 min, especially in the short-term forecasting range, where the error reduction is more evident. This suggests that the introduced residual-correction mechanism is particularly effective for ultra-short-term prediction. It should be noted that, at the 20 min and 25 min forecast horizons, several error metrics of the Cascade LSTM+RBF model are slightly higher than those of the standalone Cascade LSTM model. This implies that, as the forecast horizon increases, the effectiveness of residual correction may be jointly affected by sample-distribution changes and error-propagation mechanisms, and its gain is not necessarily uniform across all forecast steps. Nevertheless, from the overall perspective, the Cascade LSTM+RBF model still exhibits better average performance and stronger robustness.

Figure 8 presents four randomly selected examples of continuous six-step forecasting results. Compared with the standalone Cascade LSTM model, the Cascade LSTM+RBF model is more consistent with the true variation trend and provides a more accurate fit to local fluctuations as well as peak-valley changes. These results indicate that the proposed Cascade LSTM+RBF method can not only improve the accuracy of continuous multi-step forecasting of ionospheric scintillation risk, but also enhance the capability of tracking temporal variations, thereby providing effective technical support for short-term scintillation forecasting in low-latitude regions

Table 2 Comparison of eMAE, eRMSE, and eNRMSE for continuous six-step forecasting of ionospheric scintillation on the test set

Time	Recursive LSTM			Recursive LSTM+RBF			Cascade LSTM			Cascade LSTM+RBF		
[min]	MAE	RMSE	NRMSE	MAE	RMSE	NRMSE	MAE	RMSE	NRMSE	MAE	RMSE	NRMSE
5	0.73	0.95	3.87	0.69	0.89	3.66	0.71	0.92	3.77	0.68	0.88	3.61
10	0.71	0.92	3.76	0.70	0.90	3.69	0.65	0.84	3.45	0.64	0.83	3.38
15	0.69	0.90	3.68	0.66	0.86	3.52	0.60	0.70	3.24	0.59	0.79	3.22
20	0.68	0.87	3.55	0.66	0.87	3.55	0.55	0.74	3.05	0.58	0.78	3.20
25	0.65	0.83	3.39	0.63	0.83	3.39	0.58	0.78	3.21	0.61	0.81	3.31
30	0.67	0.87	3.58	0.63	0.85	3.49	0.63	0.83	3.41	0.61	0.81	3.31

Note: MAE and RMSE are expressed in TECU/min, whereas NRMSE is expressed as a percentage (%).

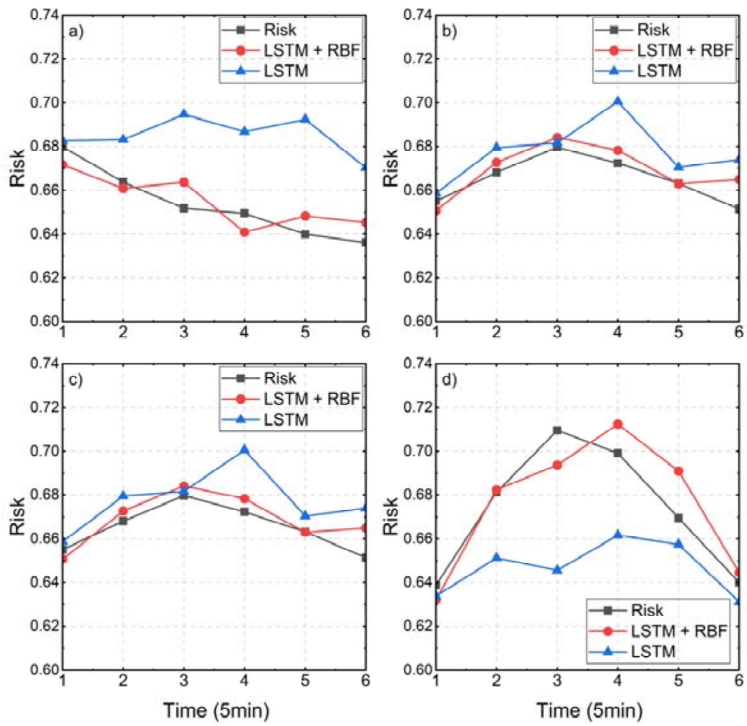

Fig. 8 Randomly selected examples of continuous six-step forecasting results of the LSTM-RBF model

To evaluate the integrity characterization capability of the proposed LSTM-RBF model in ionospheric scintillation risk forecasting, the samples were divided into the scintillation phase and the non-scintillation phase, and analyzed from two aspects: the distributional overbounding characteristics and the consistency with protection-level constraints. In the figure, the left panels show the empirical cumulative distribution functions (CDFs) of the sample risk values together with the left and right boundaries estimated by the model under different phases, while the right panels present the corresponding Stanford plots, which are used to further examine the integrity relationship between the predicted envelope and the actual residuals.

The CDF results show that, in both the scintillation and non-scintillation phases, the left and right boundaries constructed by the model can effectively overbound the sample distribution, indicating that the proposed method can adequately characterize the uncertainty range of the risk sequence. A further comparison between the two phases shows that the distance between the left and right boundaries is significantly larger during the scintillation phase than during the non-scintillation phase. This indicates that, when ionospheric disturbances intensify and risk fluctuations become stronger, the model can adaptively widen the envelope to accommodate larger random variations and more pronounced tail behavior. In contrast, during the non-scintillation phase, the boundary interval becomes relatively narrower, indicating that the model can still maintain a tight overbounding capability under relatively quiet background conditions and thus avoid excessive conservatism. These results demonstrate that the proposed method does not rely on a fixed-width envelope, but instead dynamically adjusts the protection range according to the disturbance state, thereby achieving a favorable balance between conservatism and tightness.

The Stanford plots further support this conclusion. It can be seen that the vast majority of sample points are distributed above the diagonal line $y=x$, meaning that the predicted GIVE is generally larger than the corresponding actual residual. This indicates that the constructed envelope satisfies the basic overbounding requirement for most samples and does not exhibit obvious systematic underbounding. In the scintillation phase, the sample points show a larger spread along the vertical axis, and the range of GIVE values is also wider, reflecting that the model can provide a larger protection margin under highly disturbed conditions with stronger error uncertainty. By contrast, in the non-scintillation phase, most sample points are concentrated in the region of smaller residuals and lower GIVE values, exhibiting a more compact distribution pattern. This suggests that, during relatively quiet conditions, the model can maintain a smaller protection level without unnecessarily inflating the risk. In other words, the proposed model exhibits an adaptively expanded protection characteristic during the scintillation phase, while maintaining good tightness control during the non-scintillation phase.

Taken together, the CDF and Stanford-plot results indicate that the LSTM-RBF model can not only provide continuous forecasts of ionospheric scintillation risk, but also generate an integrity-oriented overbounding envelope that is consistent with the disturbance state. This envelope remains sufficiently conservative during enhanced scintillation conditions while preserving good tightness during non-scintillation periods. These results demonstrate that the proposed method has strong integrity-characterization capability and promising engineering potential, and can provide support for GNSS risk warning and protection-level construction under ionospheric disturbance conditions in low-latitude regions.

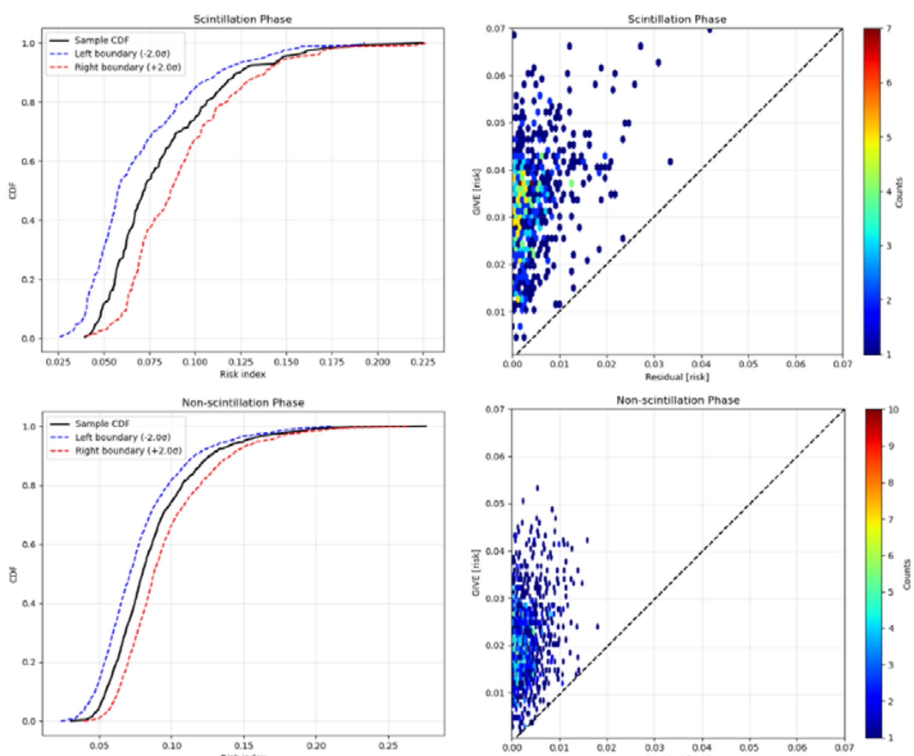

Fig. 9 Performance of the model overbounding envelope during scintillation and non-scintillation periods

5 Conclusions

This study proposed a Cascade LSTM+RBF framework for the joint short-term forecasting and integrity overbounding of low-latitude ionospheric scintillation risk. The framework was designed to address the non-stationarity, abrupt variability, and conditional heteroscedasticity of the risk sequence, as well as the limited integrity characterization provided by conventional point-forecasting models. In the proposed method, a Cascade LSTM model is first used to extract the temporal evolution trend of the risk sequence and to perform continuous ultra-short-term multi-step forecasting. An RBF network is then introduced to model the conditional mean and conditional variance of the prediction residuals. On this basis, a tight overbounding envelope can be constructed and synchronously output together with the forecast results, thereby enabling the joint characterization of ionospheric scintillation risk and its associated uncertainty.

Experimental results based on GNSS observations from a low-latitude region show that, compared with the conventional recursive forecasting strategy, the Cascade LSTM model can effectively mitigate error accumulation in multi-step recursive prediction and improve the stability and accuracy of continuous multi-step forecasting. On this basis, the RBF-based residual correction further enhances the overall predictive performance of the model. The six-step forecasting results on the test set show that the proposed Cascade LSTM+RBF model reduces the average eMAE, eRMSE, and eNRMSE by approximately 3.8%, 2.5%, and 2.3%, respectively, compared with the standalone Cascade LSTM model. These results indicate that conditional modeling of residual statistical characteristics can effectively compensate for the systematic bias that is not fully captured by the main forecasting model, thereby improving the multi-step forecasting accuracy of ionospheric scintillation risk.

Further integrity analysis shows that the overbounding envelope constructed by the proposed method can effectively enclose the actual risk distribution during both scintillation and non-scintillation periods, while exhibiting clear adaptive characteristics. During enhanced scintillation periods, the envelope appropriately expands with increasing risk fluctuations, thereby improving the capability of covering tail disturbances and abnormal variations. During non-scintillation periods, the envelope remains relatively tight, thus avoiding excessive inflation of the protection level. This adaptive characteristic is crucial for avoiding unnecessary conservatism during quiet periods, thereby preserving service availability, while still ensuring safety during active periods. The Stanford-plot results show that most sample points are located in the safe region, and the predicted GIVE is generally larger than the actual residual, indicating that the constructed envelope satisfies the basic overbounding requirement overall and does not exhibit obvious systematic underbounding. These findings demonstrate that the proposed method can not only provide continuous forecasts of ionospheric scintillation risk, but also supply integrity-relevant uncertainty bounds for the forecast results.

Overall, the proposed Cascade LSTM-RBF framework realizes integrated modeling from ionospheric scintillation risk forecasting to integrity overbounding envelope construction, and provides a new methodological basis for GNSS risk warning, protection-level assessment, and trustworthy positioning applications in low-latitude disturbed environments. Future work may proceed in three directions. First, more real-time available space-weather drivers and station-observation features can be incorporated to improve model robustness under extreme disturbance conditions. Second, the current station-level risk-forecasting framework can be extended toward regional and gridded ionospheric risk-map generation. Third, further investigation is needed into the mapping relationship among the risk index, actual GNSS positioning error, protection level, and alert limit, so as to promote the practical application of the proposed method in integrity monitoring and safety-critical navigation scenarios.

6 Acknowledgment

This research was supported by the National Natural Science Foundation of China (NSFC) (Nos. 42274021, 42361134583) and the China Postdoctoral Science Foundation (No. 2023M743762).

References

Atabati, A., Jazireeyan, I., Alizadeh, M., & Langley, R. B. (2024). Prediction of ionospheric scintillation with ConvGRU networks using GNSS ground-based data across South America. *Remote Sensing, 16*(15), 2757. https://doi.org/10.3390/rs16152757

Carvalho, O., da Silva de Almeida Nava Alves, P. A. A., de la Cruz Cueva, R. Y., & Filho, A. O. B. (2022). Nowcasting of amplitude ionospheric scintillation based on machine learning techniques. IEEE Transactions on Aerospace and Electronic Systems, 58 (6), 4917–4927. https://doi.org/10.1109/TAES.2022.3188741

Chen, S.-P., Bilitza, D., Liu, J.-Y., Caton, R., Chang, L.

C., & Yeh, W.-H. (2017). An empirical model of L-band scintillation S4 index constructed by using FORMOSAT-3/COSMIC data. *Advances in Space Research, 60*(5), 1015–1028. https://doi.org/10.1016/j.asr.2017.05.031

De Lima, G. R. T., Stephany, S., de Paula, E. R., Batista, I. S., & Abdu, M. A. (2015). Prediction of the level of ionospheric scintillation at equatorial latitudes in Brazil using a neural network. *Space Weather, 13*(8), 446–457. https://doi.org/10.1002/2015SW001182

Gao, Z., Chen, Y., Ao, X., Yue, F., Chen, H., Deng, H., Luo, B., Wang, X., and Yuan, T. (2025). ISNet: Decomposed dynamic spatio-temporal neural network for ionospheric scintillation forecasts. Space Weather, 23, e2024SW004239. https://doi.org/10.1029/2024SW004239.

Kim, M., Seo, J., & Lee, J. (2014). A comprehensive method for GNSS data quality determination to improve ionospheric data analysis. *Sensors, 14*(8), 14971–14993. https://doi.org/10.3390/s140814971

Li, W., Jiang, Y., Ji, H., & Wei, W. (2024). Amplitude scintillation detection with geodetic GNSS receivers leveraging machine learning decision tree. *Satellite Navigation, 5*, 18. https://doi.org/10.1186/s43020-024-00136-7

Luo, X., Gu, S., Lou, Y., Cai, L., & Liu, Z. (2020). Amplitude scintillation index derived from C/N0 measurements released by common geodetic GNSS receivers operating at 1 Hz. *Journal of Geodesy, 94*(2), 27. https://doi.org/10.1007/s00190-020-01359-7

Mao, S., Pan, Y., Kłopotek, G., Schartner, M., Krásná, H., de Witt, A., and Soja, B. (2025). Enhanced global ionospheric mapping using deep ensemble neural networks with uncertainty quantification. Space Weather, 23, e2025SW004446. https://doi.org/10.1029/2025SW004446.

McGranaghan, R. M., Mannucci, A. J., Wilson, B., Mattmann, C. A., & Chadwick, R. (2018). New capabilities for prediction of high-latitude ionospheric scintillation: A novel approach with machine learning. *Space Weather, 16*, 1817–1846. https://doi.org/10.1029/2018SW002018

Monte-Moreno, E., Yang, H., and Hernández-Pajares, M. (2026). Global ROTI forecasting with a Bayesian model based in long-tail distributions. Satellite Navigation, 7, 1. https://doi.org/10.1186/s43020-026-00188-x

Nikiforov, I. (2019). From pseudorange overbounding to integrity risk overbounding. *Navigation, 66*(2), 417–439. https://doi.org/10.1002/navi.303

Oljira, A. (2023). A study of solar flares and geomagnetic storms impact on total electron content over high-latitude region during July–November 2021: The case of Tromso station. *Advances in Space Research, 72*(9), 3868–3881. https://doi.org/10.1016/j.asr.2023.06.051

Ojo, O. L., Abe, O. E., Hammed, O. S., and Olumodimu, O. A. (2025). Short-time forecast of ionospheric irregularities using long short-term memory networks over equatorial and low-latitudes regions. Journal of Atmospheric and Solar-Terrestrial Physics, 269, 106466. https://doi.org/10.1016/j.jastp.2025.106466.

Pi, X., Mannucci, A. J., Lindqwister, U. J., & Ho, C. M. (1997). Monitoring of global ionospheric irregularities using the worldwide GPS network. *Geophysical Research Letters, 24*(18), 2283–2286. https://doi.org/10.1029/97GL02273

Sridhar, M., Venkata Ratnam, D., Padma Raju, K., Sai Praharsha, D., & Saathvika, K. (2017). Ionospheric scintillation forecasting model based on NN-PSO technique. *Astrophysics and Space Science, 362*(9), 166. https://doi.org/10.1007/s10509-017-3144-6

Tete, S., Otsuka, Y., Zahra, W. K., & Mahrous, A. (2024). Leveraging machine learning techniques and GPS measurements for precise TEC rate predictions. *GPS Solutions, 28*(3), 115. https://doi.org/10.1007/s10291-024-01652-4

Vadakke Veettil, S., & Aquino, M. (2021). Statistical models to provide meaningful information to GNSS users in the presence of ionospheric scintillation. *GPS Solutions, 25*(2), 54. https://doi.org/10.1007/s10291-020-01083-x

Wang, J., & Morton, Y. T. (2017). A comparative study of ionospheric irregularity drift velocity derived from a GNSS receiver array and Poker Flat incoherent scatter radar measurements during high-latitude ionospheric scintillation. *Journal of Geophysical Research: Space Physics, 122*(6), 6858–6881. https://doi.org/10.1002/2017JA024015

Xu, F., Li, Z., Zhang, K., Wang, N., Wu, S., Hu, A., & Holden, L. (2020). An investigation of optimal machine learning methods for the prediction of ROTI. *Journal of Geodesy and Geoinformation Science, 3*(2), 1–15.

Zhao, D., Cui, S., Zhang, X., Li, L., Sun, P., Bian, C., Ban, W., Hancock, C. M., Wang, Q., & Zhang, K. (2024). Analysis of global ionospheric scintillation and GPS positioning interference triggered by full-halo CME-driven geomagnetic storm: A case study. *Advances in Space Research, 74*(5), 2492–2509. https://doi.org/10.1016/j.asr.2024.06.001

Zhao, D., Li, W., Li, C., Hancock, C. M., Roberts, G.

W., & Wang, Q. (2022). Analysis on the ionospheric scintillation monitoring performance of ROTI extracted from GNSS observations in high-latitude regions. *Advances in Space Research, 69*(1), 142–158. https://doi.org/10.1016/j.asr.2021.09.026

Zhao, D., Roberts, G. W., Hancock, C. M., Lau, L., & Bai, R. (2019). A triple-frequency cycle slip detection and correction method based on modified HMW combinations applied on GPS and BDS. *GPS Solutions, 23*(1), 22. https://doi.org/10.1007/s10291-018-0817-8

Zhang, Y., Xiao, Z., Li, P., Tang, X., and Ou, G. (2019). Conservative Sensor Error Modeling Using a Modified Paired Overbound Method and its Application in Satellite-Based Augmentation Systems. *Sensors*, 19(12), 2826. https://doi.org/10.3390/s19122826.

Authors

Hao Liu is currently pursuing his PhD degree at China University of Mining and Technology. His research interests include ionospheric scintillation monitoring, forecasting, and GNSS positioning integrity.

Dongsheng Zhao is a Specially Appointed Research Fellow at the School of Environment and Spatial Informatics, China University of Mining and Technology. He received his Ph.D. degree from the University of Nottingham and his B.Eng. degree from Wuhan University. His research focuses on GNSS remote sensing, particularly ionospheric scintillation monitoring and modeling.

Kefei Zhang is a Professor at the School of Environment and Spatial Informatics, China University of Mining and Technology. He received his Ph.D. degree from Curtin University, Australia. His research interests include GNSS atmospheric modeling, space mining and precision agriculture.

Ke Xu is currently a master's student at China University of Mining and Technology. Her research interest is ionospheric scintillation monitoring and modeling.

Qichen Zhao is currently a master's student at China University of Mining and Technology. His current research focuses, mainly involve GNSS precise positioning.